Simulation and Validation of CFD turbulent air flow at pedestrian level using 3D ultrasonic anemometer in the controlled urban area "Sense-City"

Benjamin Streichenberger, Rachida Chakir, Bastien Jouy, Julien Waeytens

Simulation and Validation of CFD turbulent air flow at pedestrian level using 3D ultrasonic anemometer in the controlled urban area "Sense-City"

Benjamin Streichenberger[a,*], Rachida Chakir[a,b,*], Bastien Jouy[a], Julien Waeytens[a,b]

[a] *Université Gustave Eiffel, IFSTTAR, Marne-la-Vallée, France*
[b] *Efficacity, Marne-la-Vallée, France*

Abstract

Computational Fluid Dynamics (CFD) is increasingly used to describe the airflow in urban environments. However, it lacks of real-scale validations with sensor outputs. In this study, we aim to simulate and to validate the airflow in a full-scale urban area named "Sense-City" – an uncommon equipment made up of a 400 m^2 realistic district with buildings and street network. In addition, a climatic chamber can enclose the district in order to control the climatic conditions. The Sense-City urban area is highly instrumented, which allows notably the validation of physical models and simulations. Using a URANS model, with the k-omega SST model as the closure model, a CFD analysis is made on the turbulent airflow in Sense-City at a reasonable computational cost. The simulated velocities and turbulent kinetic energy are compared with measurements collected at a pedestrian level using a 3D ultrasonic anemometer. We show that the numerical simulations correctly predict the flow direction and flow characteristics such as dead flow zones. Geometry simplifications, uncertainties on the boundary conditions and the use of a coarse mesh and time discretization to fulfill operational purposes have led to a Root Mean Square Error (RMSE) score of 0.26 m/s on the velocity magnitude.

Keywords: Computational Fluid Dynamics, Turbulent flow, Experimental validation, Full-scale measurement, Anemometer, Sense-City

1. Introduction

A wide range of studies in urban design and planning relies on a good knowledge of airflow pattern and velocity field. Indeed, detailed information are often required in the evaluation of air quality and pollutant dispersion, cooling of

*Corresponding author
Email addresses: benjamin.streichenberger@univ-eiffel.fr (Benjamin Streichenberger), rachida.chakir@univ-eiffel.fr (Rachida Chakir)

building using natural ventilation, pedestrian comfort in area with high density building, evapotranspiration of plants and trees, etc. Advances made in numerical methods and computational powers have enabled the use of Computational Fluid Dynamics (CFD) models in simulation at building and district scales. The most commonly used CFD Turbulence models can be classified into two categories: Steady or unsteady Reynolds Averaged Navier-Stokes (RANS or URANS, see [40]) and Large Eddy Simulation (LES, see [41]). Despite their lack of accuracy compared to LES model [17], RANS models remain largely used in operational studies due to their lower computational cost [6].

In indoor environment, CFD models are widely applied, notably for air quality and thermal building purposes. For example, it was considered in the prediction of indoor airflow pattern and temperature [24, 10], the humidity distribution into an indoor swimming pool [31], the dispersion of a heavy gas due to an incident in a factory [14] and the design of intensive care units in a hospital dedicated to burn victims [5]. Regarding outdoor environment, CFD have been used in urban areas in order to get a better understanding of the airflow and the pollutant dispersion [37, 17, 22]. In the literature, a special attention has been given to street canyons [28, 12] taking into account turbulences induced by traffic [44], the roof shapes [50] and the vegetation [42, 4, 19]. An overview is proposed in the review article [30].

CFD analysis can be considered as a promising numerical tool to evaluate, via virtual testing, different strategies of urban planning. In [18], CFD simulations were made at a district scale to quantify the cooling effect, during a heat wave, of several revegetation scenarios such as tree planting and wall and/or roof vegetation. In [7], the authors used CFD models to evaluate airflow pattern in a large stadium and the possible adverse effects in wind pedestrian comfort due to the construction of new high-rise buildings nearby. In the last decade CFD has also become a popular tool for studying wind-driven natural ventilation efficiency in buildings. The influence of balconies [35], position and shape of openings [36, 27] and other building specificities are evaluated through numerical analysis. In addition, CFD can be an affordable tool for the decision-making process and the urban design of innovative solution such as depolluting systems based on ZnO photocatalysis reaction [29, 15]. Lastly, CFD analysis can improve the selection of gas sensor location and their number [46, 45], and provide adapted and optimal sensor placement for data-assimilation [21].

Most of the cited articles rely on wind tunnel experiments for the validation of the CFD simulations. Unfortunately, real-scale field experiments in an urban area are rarely considered, despite being necessary especially when improving the reliability of CFD models through data assimilation techniques [25, 20]. Therefore in this paper, the focus is on the real-scale validation and simulation of an urban airflow. The simulations are performed using a URANS turbulent model. The experiments are conducted under controlled conditions in an uncommon full-scale climatic chamber named "Sense-City" and 3D ultrasonic anemometers are used for model validation. Let us note that three dimensional anemometers were used as a reference velocity measurement to validate LIDAR-based sensor [8]. Anemometers were also considered for the comparison

of experimental and numerical mean flow and turbulence characteristics [32, 47], the study of interactions between the meteorological conditions and the air pollution [43] and the turbulence induced by vehicles traffic [2].

The article is organized as follows. First in Section 2, a detailed description of the climatic chamber and the real-scale urban area built in Sense-City are given. In Section 3 the CFD model and the computational settings are specified. Section 4 deals with a convergence error analysis in order to choose the appropriate simulation to compare with the experimental data. Section 5 focuses on the comparison between the experimental values collected with 3D ultrasonic anemometers and the CFD simulation results. Finally, in Section 6, concluding remarks and perspectives are given.

2. Sense-City equipment for real-scale experiments

Sense-city is an Equipment of Excellence funded by the French National Research Agency (ANR). It is designed for the testing and the demonstration of innovative technologies in real or controlled urban environments. In this section we briefly present the facilities and the characteristics of the climatic chamber.

2.1. Presentation of Sense-City

The platform Sense-City (figure 1) is made of a $3200\,\mathrm{m}^3$ climatic chamber and two instrumented full-scale urban area of $400\,\mathrm{m}^2$ each ($20\,\mathrm{m} \times 20\,\mathrm{m}$), named *mini-city 1* & *mini-city 2*. The climatic chamber provides a controlled environment and is mounted on rails in order to move from one *mini-city* to the other. It is designed to replicate real weather conditions with temperature ranging from $-10°\mathrm{C}$ to $40°\mathrm{C}$, humidity ranging from 20% to 95%, rain events, sun exposure and air pollution.

Figure 1: View of the climatic chamber (left) and the *mini-city 1* covered by the climatic chamber (right)

The *mini-city 1* was built on a 1000 m^3 waterproof pit filled with mastered natural soil. Launched in April 2018, this *mini-city 1* includes a wooden house, a small house made of bio-based materials and a two-story precast concrete building, a street network (including sidewalk, street lighting, crosswalk and traffic light). It is instrumented with more than 150 permanent sensors spread between the underground, the building's facade, the indoors and the outdoor. This includes 60 temperature sensors and 30 sensors for air pollution monitoring, starting from Particule Matter (PM) and Volatile Organic Compound (VOC) to gases such as NO_2, O_3, CO, and CO_2. A weather station is fixed at the top of the two-story building to measure the temperature, humidity and wind speed and direction. All those sensors are plugged into *PEGASE* data acquisition cards that send the measured data to a web server through a WiFi connection. With its various devices, the Sense-City platform provides an experimental environment for a wide variety of societal urban problems from sustainable water network, soil pollution and indoor or outdoor air quality, to building energy efficiency. In previous works, Sense-City was notably used for a geothermal application [11], a micro-grid study [39] and the validation of an inverse technique applied to a thermal building problem [13].

2.2. Characteristics of the climatic chamber

The airflow temperature and humidity within the climatic chamber are ensured by a system combining twelve blocks of fans and two sets of suction and forced-air ducts (see figure 2) distributed over the south and north walls of the chamber. Each block of fans is formed with three axial fans; each set of ducts is made up of two perforated horizontal pipes of 18 m length for forced-air ventilation and two vertical columns for air extraction. For each set of suction and forced-air ducts, the ventilation system works as follows: the airflow is extracted at the bottom of the columns and split between the two horizontal pipes (see figure 3). The latter are perforated with circular holes of varying diameters from which the airflow is spread in angle. These forced-air ducts are designed to homogenize the temperature inside the climatic chamber. Concerning the twelve blocks of fans, they are designed to control the temperature (heating or cooling), and two of them work also as dehumidifiers.

In this work, our goal is to compute the 3D airflow pattern and velocity field in the *mini-city 1* within the climatic chamber environment. To this end, we need information on the inflow and outflow of the climatic chamber. A first experimental study was carried out with a 1D hot wire anemometer to measure the velocity values at the different inlets/outlets of the ventilation system as shown in figure 2. Starting with the blocks of fans, we took several velocity measurements to estimate the volumetric flow rate of each fan. Let us note that the fans of the two blocks designed as dehumidifiers have a reduced flow rate compared to the other fans. We measured a total rate of $Q_{\mathrm{r}} = 5.7\ m^3/s$ for those two blocks. For the ten remaining blocks, the total airflow rate is $Q_{\mathrm{f}} = 66.0\ m^3/s$. Hence, the flow rate of a reduced speed block represents about 45% of the flow rate of a regular block. Concerning the suction and forced-air ducts system, we started by measuring the velocity of the extracted air at the

Figure 2: Partial view of the chamber ventilation system, including blocks of fans and a part of a set of suction and forced-air ducts. Picture taken during an experiment to measure the inflow velocities of the ventilation system of the climatic chamber using a 1D hot wire anemometer.

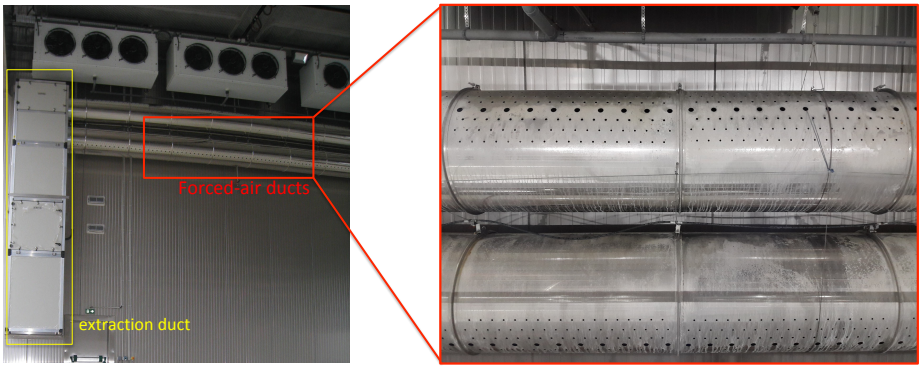

Figure 3: Detailed view of a part of the suction and forced-air ducts system.

bottom of the four extraction ducts positioned at each corner of the climatic chamber and found a total rate of $Q_{\mathrm{s}} = 15.3\ m^3/s$. Then, we measured the flow passing through holes of the forced-air ducts to evaluate the airflow distribution between the lower and upper ducts (see figure 3). We noted that the lower ducts have a higher flow rate than the upper ducts, approximately 55% of the total flow rate extracted by the extraction duct. Therefore the upper forced-air ducts have a total flow rate of $Q_{\mathrm{u}} = 6.9\ m^3/s$, and the lower forced-air ducts have a total rate of $Q_{\ell} = 8.4\ m^3/s$. All these volumetric airflow rates summarized in

table 1 are used as input parameters in the CFD simulation.

Ventilation components	Total airflow rate	Value (m^3/s)
Extraction ducts	Q_s	15.3
Upper forced-air ducts	Q_u	6.9
Lower forced-air ducts	Q_ℓ	8.4
Fans with reduced airflow	Q_r	5.7
Regular fans	Q_f	66.0

Table 1: Total airflow rates of the inlet/outlet components of the climatic chamber ventilation system

3. CFD model

In this section, we introduce the computational domain, the physical model and the computational settings chosen for the simulation.

3.1. Computational Domain

In our approach, we choose to not simulate the airflow inside the ventilation system; instead we compute only the airflow in the *mini-city 1* within the climatic chamber of Sense-City and impose boundary conditions to represent the effect of the ventilation system. The figure 4 illustrates the geometry considered for the CFD simulations. The *extraction* parts of the fans are colored in green; the *inflow* sides are colored in blue for the fans with a reduced flow rate and in red for those with a normal flow rate. The extraction surfaces of the suction ducts are colored in yellow. The perforations of the forced-air ducts are colored in white for the upper ducts and in pink for the lower ducts.

In practice, we choose to neglect geometrical details (e.g. sidewalks, street signs and traffic light,...) that would only have had a small effect on the airflow pattern. To limit the number of cells and thus the computational cost, we have replaced the series of circular holes in the perforated forced-air ducts (see figure 3) by a sequence of rectangular slots (see figure 4). This choice of simplification is made in order to preserve the vertical repartition of the perforation. The modeling of the blocks of fans is also simplified: a disk of radius 0.1m is used to represent the center of the axial fans with a zero velocity.

3.2. CFD modeling

In this work, we use a CFD model to compute the airflow in the *mini-city 1* within the climatic chamber. To set up our model, namely the boundary conditions, the selection of a turbulence model and the choice of a reliable grid, we followed the recommendations and guidelines found in [6] and [16]. We assume that the air flow inside the climatic chamber is Newtonian and incompressible. The temperature variations are neglected as a 20^oC constant

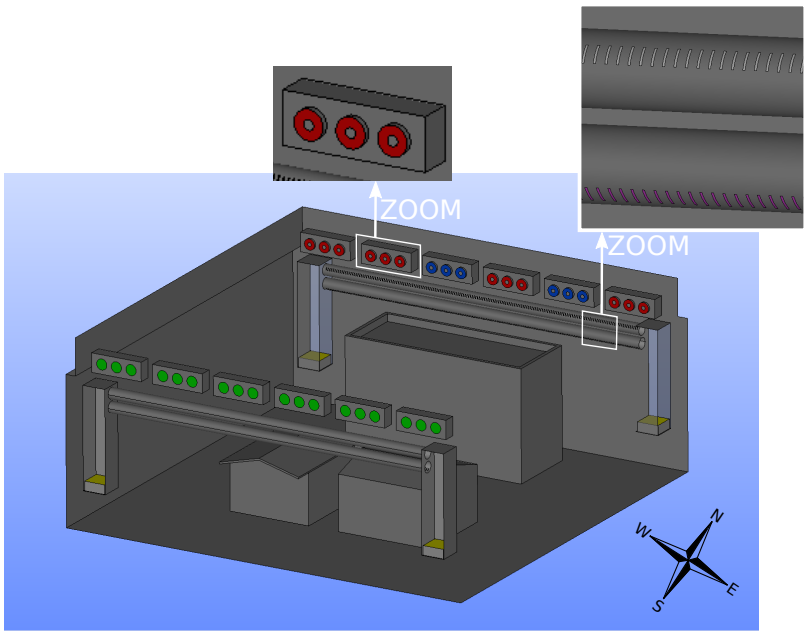

Figure 4: Simplified geometry of the *mini-city 1* within the climatic chamber of Sense-city

temperature is imposed in the climatic chamber and the sun lights are turned off. Besides, due to the high variability induced by turbulent phenomena around the structures (building, houses and climatic chamber walls), we expect the airflow to be highly three-dimensional and unsteady. Therefore, the simulations are made with a 3D and unsteady Reynolds Averaged Navier-Stokes (RANS) model. The considered governing equations are the Navier-Stokes equations with the k-omega SST turbulence closure model. Although LES modeling is known to give better predictions and accuracy (at expensive computational cost) than RANS modeling, we choose to use the latter mainly because, in the CFD community, RANS is still widely more applied than LES, (see [6]) notably by engineers, and we want this study to provide some guidelines for futures CFD simulations in small urban areas. In fact, the relevance of the turbulence model choice in model accuracy for CFD simulations is only significant when other sources of errors, such as numerical and convergence errors, or input and boundary errors, have been controlled.

The k-omega SST turbulence model was introduced in [33] by Menter in 1994 and continually improved over the years [49]. It combines the $k-\epsilon$ turbulence model [26], [34] away from the walls and the classic $k-\omega$ turbulence model [48] in the boundary layers. The $k-$omega SST model is very accurate near the walls, it predicts reattachment better than the standard $k-\omega$ model and it is also less sensitive to boundaries conditions, which makes this choice more

relevant in this study.

We denote by Ω the computational domain, Γ the boundary domain, Γ_{in} the inlet boundaries, Γ_{out} the outlet boundaries and $\Gamma_{\text{wall}} = \Gamma \setminus \{\Gamma_{\text{in}} \cup \Gamma_{\text{out}}\}$ as the wall boundaries. We enforce non-homogeneous Dirichlet conditions on Γ_{in} and Γ_{out} and a no-slip condition on Γ_{wall}. For the Dirichlet conditions, we use the values of the volumetric airflow rate summarized in table 1.

3.3. Computational settings

As explained previously, a k-omega SST turbulence model belonging to RANS category is considered to simulate the 3D unsteady air flow. All the equations are discretized according to the Finite Volume method. The CFD software CODE_SATURNE [3] is used with the option single phase flow. The SIMPLE algorithm is applied to deal with the pressure-velocity coupling. The gradient calculation is performed with a Least Squares method based on a partial extended neighborhood. For all the other numerical parameters in CODE_SATURNE we kept the default values, with the exception of the velocity convective term calculation where a Second Order Linear Upwind (SOLU) scheme was used (which is more suited to the unsteady nature of the simulation). The time-schemes are all of first-order accuracy with a constant time step. The stopping criterion is the number of time steps, which gives us a fixed simulation time. To mimic the experiment (see the section 5), we choose a simulation period of twenty minutes and the solutions that we compare with the measurements are averaged over the last ten minutes.

4. From mesh generation to reliable simulation

4.1. Grid convergence analysis

In addition to the choice of the CFD model and its computational settings, the mesh quality highly impact the accuracy of the simulation. In order to estimate the mesh quality, we perform a mesh error analysis. Thus, we generated six unstructured meshes of the geometry using the open-source software SALOME [38] (with the automatic mesh generator NETGEN). We choose to use unstructured meshes because of the complexity of the climatic chamber geometry. The characteristics of these meshes are summarized in table 2. The finest mesh is denoted by $\mathcal{T}_1$ and the coarsest one by $\mathcal{T}_6$. For each mesh, the first property to vary is the maximum mesh element size, which is a mesh generator parameter that represents the maximum linear dimensions for mesh cells. We have also allowed local size to vary on some geometrical objects : the inlet/outlet sections of fans, forced-air slots and air extractor sections of suction ducts. Those variations are proportionate to the maximum mesh size.

Mesh Name	Maximum mesh size [m]	Local mesh size on fans [m]	Local mesh size on forced-air slots [m]	Local mesh size on air extractors [m]	Number of cells
$\mathcal{T}_1$	0.2	0.05	0.015	0.15	3 928 240
$\mathcal{T}_2$	0.3	0.075	0.0225	0.225	1 351 002
$\mathcal{T}_3$	0.4	0.1	0.03	0.3	910 157
$\mathcal{T}_4$	0.5	0.125	0.0375	0.375	625 787
$\mathcal{T}_5$	0.6	0.15	0.045	0.45	490 295
$\mathcal{T}_6$	0.8	0.2	0.06	0.6	379 802

Table 2: Meshes characteristics

It is important to note that the maximum mesh size is not the linear dimensions of every tetrahedra of the considered mesh. This is why the refinement factor, derived from Eq. (1), between for example the meshes $\mathcal{T}_1$ and $\mathcal{T}_3$ is less than two. Indeed, there are some regions in the geometry where cells finer than the maximum authorized cells are generated, *e.g.* near some parts of the walls due to smaller details in the buildings structure. To measure the refinement factor between the different meshes, we introduce an appropriate mesh size h (see [9]) :

$$h = \left(\frac{1}{N} \sum_{i=1}^{N} \Delta V_i \right)^{\frac{1}{3}} \tag{1}$$

where N is the number of cells of the considered mesh and ΔV_i is the volume of the i-th cell. In table 3, we summarize the values of h for the different meshes $\mathcal{T}_i, 1 \leq i \leq 6$.

Mesh Name	$\mathcal{T}_1$	$\mathcal{T}_2$	$\mathcal{T}_3$	$\mathcal{T}_4$	$\mathcal{T}_5$	$\mathcal{T}_6$
Mesh size h [m]	0.10	0.15	0.17	0.19	0.21	0.23

Table 3: Mesh size h of the different meshes used in the error analysis

The aim of this error analysis, is to select the appropriate mesh for the simulations to be compared with the experimental sensor outputs, namely a mesh providing an accurate numerical solution at a reasonable computational cost

We define a reference velocity u_{ref} computed on the finest mesh $\mathcal{T}_1$, which will be considered as the reference mesh and noted $\mathcal{T}_{\text{ref}}$ in the remaining of the paper. For the calculation of u_{ref}, we took a time step equal to $\Delta t = 0.05\ s$ and a number of iterations equal to $n_{\text{iter}} = 24000$, which gives us a Courant number lower than 10 in spatial average. Let $u_i, 2 \leq i \leq 6$, be the velocity solutions

computed on the meshes $\mathcal{T}_i, 2 \leq i \leq 6$. For the calculation of theses solutions, the time step varies in proportion to the meshes characteristics (given in table 2) in order to keep the Courant number almost constant. We denote by $\overline{u}_{ref}$ and $\overline{u}_i$ the velocity solutions averaged over the last 10 minutes.

In what follows, the relative errors between $\overline{u}_{\text{ref}}$ and the velocities $\overline{u}_i, 2 \leq i \leq 6$, are compared in order to select the most suitable mesh for our study. We compute the following relative error :

$$e_i = \frac{\sqrt{\left(\mathcal{I}(u_i^x) - u_{\text{ref}}^x\right)^2 + \left(\mathcal{I}(u_i^y) - u_{\text{ref}}^y\right)^2 + \left(\mathcal{I}(u_i^z) - u_{\text{ref}}^z\right)^2}}{\sqrt{||u_{\text{ref}}^x||_{L^2}^2 + ||u_{\text{ref}}^y||_{L^2}^2 + ||u_{\text{ref}}^z||_{L^2}^2}} \tag{2}$$

where $(u_{\text{ref}}^x, u_{\text{ref}}^y, u_{\text{ref}}^z)$ and respectively (u_i^x, u_i^y, u_i^z) are the (x, y, z) - components of the velocity vectors $\overline{u}_{\text{ref}}$ and $\overline{u}_i$. The operator $\mathcal{I}$ is an interpolation operator on the reference mesh. The interpolation of the averaged velocities $\overline{u}_i$ on the reference mesh and the computation of the errors e_i were performed using the open-source PDE solver Freefem++ [23]. All these relative errors are measured in L^2-norm and plotted in the figure 5 as a function of the ratio h_{ref}/h_i, where h_{ref} is the mesh size of $\mathcal{T}_{\text{ref}}$ and h_i is the mesh size of $\mathcal{T}_i$, for $2 \leq i \leq 6$. The more this ratio is close to one, the more the mesh $\mathcal{T}_i$ is close to $\mathcal{T}_{\text{ref}}$.

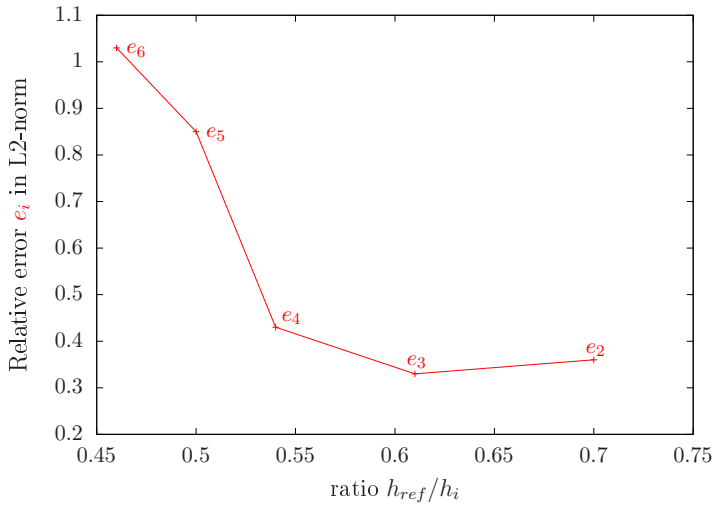

Figure 5: Velocity relative errors e_i between the reference mesh $\mathcal{T}_{\text{ref}}$ and the other meshes $\mathcal{T}_i$ with respect to the ratio $\text{h}_{\text{ref}}/\text{h}_i$, for $2 \leq i \leq 6$.

We can see a rapid decrease of the error e_i as we refine the mesh $\mathcal{T}_i$ and the time step. The more we get close to $\mathcal{T}_{\text{ref}}$, the more the relative error is small. But it seems that we reach a threshold with the mesh $\mathcal{T}_3$. Indeed, the relative error e_2 is marginally higher than e_3. Therefore, we consider that from the mesh

$\mathcal{T}_3$, the solution does not depend anymore on the mesh and time discretizations. To sum up, the mesh $\mathcal{T}_3$ is considered from now as the appropriate mesh and is noted $\mathcal{T}_h$ for the remaining of the paper. The associated time step is $\Delta t = 0.1\,\mathrm{s}$.

4.2. CFD Analysis of the airflow characteristics

To characterize the airflow around the *mini-city 1* within the climatic chamber of Sense-city, we run a 3D simulation with the selected mesh $\mathcal{T}_h$ and the time step $\Delta t = 0.1\,\mathrm{s}$. The numerical velocity solution associated is noted u_h and the numerical turbulent kinetic energy is noted k_h. To be consistent with the experiment described in the next section, we actually consider the time averaged solutions $\overline{u}_h$ and $\overline{k}_h$ for the CFD analysis. The post-processing and 2D representations were done with PARAVIEW [1]. A cross-section slice along the z-axis is performed at a pedestrian level $z = 1.5\ m$ from the ground as all the experimental values were measured in the same plane $z = 1.5\mathrm{m}$.

Herein, we are interesting in the cartography of the simulated velocity and Turbulent Kinetic Energy (TKE). From the simulations, we choose the locations of the measurement points, so that they provide specific information on the airflow pattern, for example to outline regions in the domain where a component of the velocity is close to zero. Sixteen locations are thereby selected (see figures 6 and 7) to analyze the vertical and horizontal components of the velocity, as well as the Turbulent Kinetic Energy at a pedestrian level of 1.5 m.

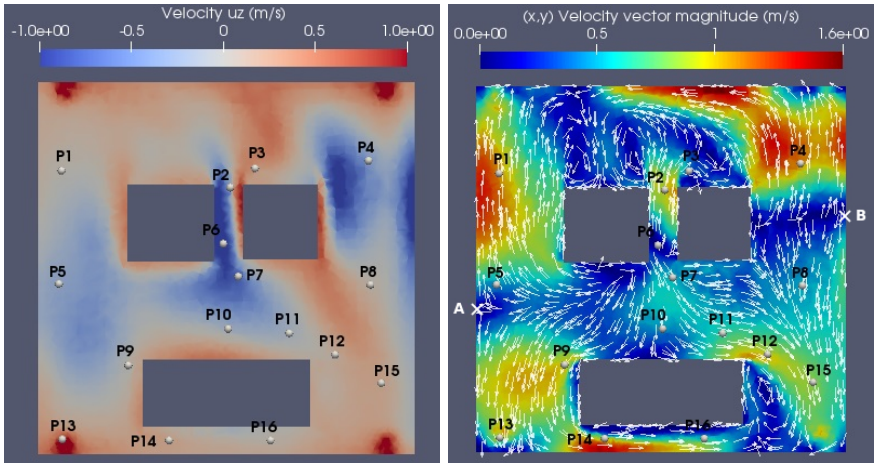

Figure 6: 2D-slice in the $x - y$ plane at $z = 1.5\mathrm{m}$. Vertical component (left) and horizontal component (right) of the simulated velocity vector $\overline{u}_h$. Representation of the measurement points.

The vertical and horizontal components of the velocity vector are represented in figure 6. The four areas at the corners of the climatic chamber present high velocity especially in the z-direction (vertical component) which is due to the air

extraction of the four suction ducts. In figure 6 (left), the blue color indicates a downslope flow going from the top of the climatic chamber to the ground, which occurs in the area between the two-story building and the houses, whereas the red color corresponds to a upslope flow which can be observed in the corners of the climatic chamber and around the building. Concerning the horizontal component of the velocity, we can see a flow separation defined by a line passing through the points 'A' and 'B' in figure 6 (right). Above (resp. below) this line the airflow is oriented in positive (resp. negative) y-direction. Concerning the building, the flow hits the north face which leads to a dominant and positive z-component (vertical) velocity. Then the flow bypasses the building from the east and the west sides. Finally, behind the building (north face) the simulation indicates a flow going from the left to the right with a strong and predominant positive x-contribution of the velocity.

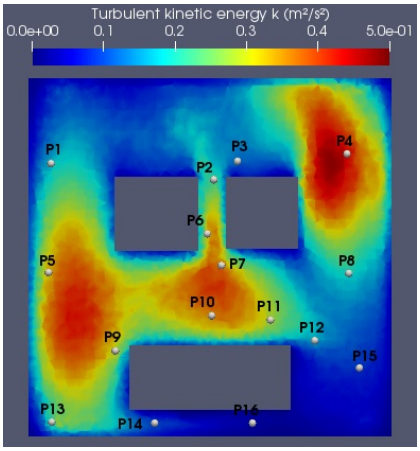

Figure 7: Map in the $x-y$ plane at $z = 1.5\ m$ of the simulated turbulent kinetic energy $\overline{k}_h$ in m^2/s^2. Representation of the measurement points.

A cross-section in the plane $(x-y)$ of the numerical solution $\overline{k}_h$ of the turbulence closure equations at the pedestrian level $z = 1.5m$ is represented in figure 7. One observe that the highest turbulent kinetic energy appears generally where the flow is downslope. In practice, the turbulent kinetic energy can also be measured using for example an anemometer (see Section 5) and this information is particularly useful for the turbulent diffusion of pollutants in air quality purposes at the district scale.

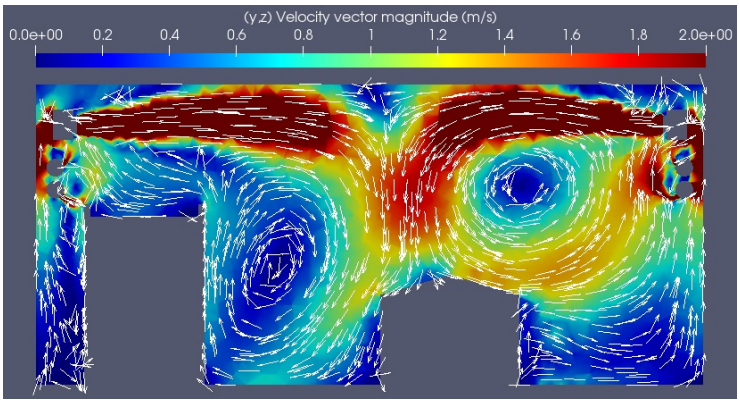

Figure 8: Cross-section in the plane $x = -1\ m$ of the magnitude of the $y - z$ velocity vector

In figure 8, one can see that the two flows generated by the fans facing each other, collide at the center of the chamber and create rotating flows and eddies. As expected, we also note that regions where the velocity magnitude is close to zero are around the building and to the right of the houses. Let us note that the forced-air above the building reproduces (between the building and the house) the airflow pattern observed in street canyons. Indeed, the flow goes down from the wall of the house to the road, then goes up at the wall of the building and keeps on recirculating.

From this CFD analysis, we choose the points of interest represented in figures 6 -7 for the following reasons:

- P1, P2, P8, P9, P11, P12 to verify the 2D horizontal behaviour of the flow in the plane $(x - y)$ (almost null vertical component) for these points;
- P14, P16 to validate the x-positive flow direction behind the building;
- P1, P2, P5 to verify that the flow is almost unidirectional in y-direction;
- P6, P7 to verify that the flow is almost unidirectional with a dominant vertical component;
- P13 have been placed under an air extractor to check its suction capacity;
- P1, P4 and P15 to verify that the x-contribution of the velocity is close to zero;
- P4, P7, P10 as the positions where the turbulent kinetic energy is the highest;
- P3 as a dead flow zone.

5. Experimental validation using 3D ultrasonic anemometers

5.1. Experimental protocol

During the experiments, a target air temperature of 20^oC was set within the climatic chamber. The sun lights of the Sense-City equipment were turned off and no humidity setpoint was considered. A 3D ultrasonic anemometer (*CSAT-3B* sensor model) and a *CR6* data acquisition system were used to measure the flow at the points of interest in the district Sense-City – points chosen from the CFD analysis and represented in figures 6 and 7. The *CSAT-3B* sensor allows to measure the 3 components of the velocity within a measurement error in the x and y- directions (resp. in z direction) of $\pm 0.08\ m/s \pm 5\%$ of reading (resp. $\pm 0.08\ m/s \pm 5\%$). The experimental values of the velocity and the Turbulent Kinetic Energy are obtained using the following process of measurement:

1. Place the 3D anemometer at a given position in the district as depicted in figure 9. Note that the anemometer is pointed into the prevailing wind, determined from CFD analysis, to minimize interference from the anemometer support structure.

Figure 9: Picture of the 3D ultrasonic anemometer (*CSAT-3B* sensor model) placed at the position P9 as defined in figure 6.

2. Launch the acquisition at a 50 Hz frequency and leave the climatic chamber of Sense-City.
3. Record the data during 20 minutes. The flow being disrupted by our presence, the first 10 minutes of data are removed and only the last 10 minutes are exploited. In figure 10, a typical time evolution of the measured turbulent velocity in the district Sense-City is represented. This output was obtained with an anemometer placed at the position P9 (see figure 6). We note that the flow is dominant in the x-direction with a mean value of

1.22 m/s, the y-component of the velocity is negative with strong variations, *i.e* $\sigma_y = 0.4\ m/s$, and in the vertical direction z the component is close to 0.

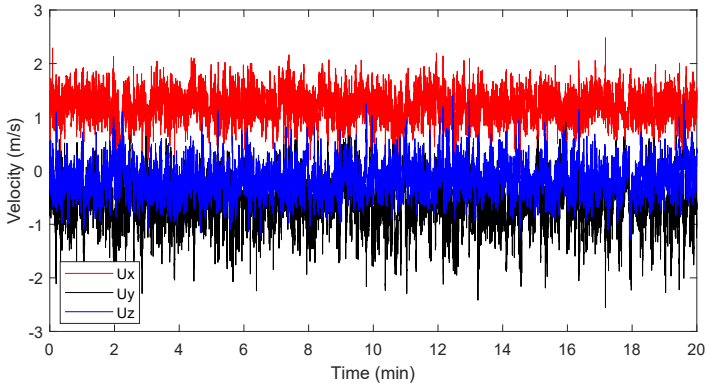

Figure 10: Measured velocity on a 20 min time interval from the 3D ultrasonic anemometer placed at the position $n^o 9$.

4. Compute the averages of the velocity $\bar{u}^m$ and the turbulent kinetic energy k^m using the sensor outputs from the 10 last minutes. In practice, k^m is evaluated by:

$$k^m = \frac{1}{2}(\sigma_x^2 + \sigma_y^2 + \sigma_z^2) \tag{3}$$

where σ_j^2 is the variance of the velocity outputs acquired on the 10 last minutes time interval for the j-th component.

5.2. Comparison of measured and simulated turbulent flow

From the CFD analysis, 16 positions of interest were selected to represent the wide variety of the encountered flow in the district *mini-city 1* of Sense-City. Indeed, a null-velocity flow can be observed at some points and dominant flow in a given direction can be noted in another points. The 16 positions, represented in the figures 6 and 7, are all in the same $x - y$ plane at a pedestrian level of 1.5 m from the ground.

The experimental protocol presented in the previous section is reproduced for each of the listed sensor positions. The series of measurement were conducted during a whole day in July 2019. The conditions being fully controlled in the climatic chamber, the measured flow does not depend on the time period of the day. In figure 11, we show a comparison between sensor outputs and numerical simulations for the velocity components and for the turbulent kinetic energy at the 16 points of measurement. Besides, global statistical performances are given in table 4 (definition of the statistical scores are given in Appendix). The sensor outputs and the numerical results are provided in the supplementary

file “ResultSynthesis.txt”.

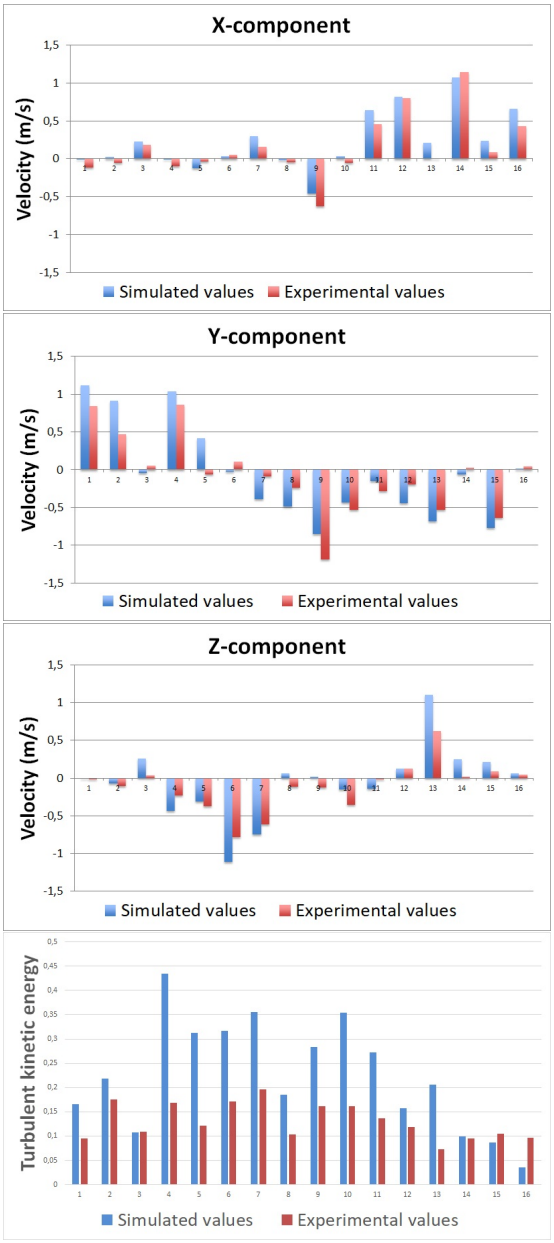

Figure 11: Comparison at the 16 measurement points between sensor outputs and numerical simulations for the x-component of the velocity, the y-component of the velocity, the z-component of the velocity and for the turbulent kinetic energy.

	BIAS	RMSE	NRMSE
Horizontal flow direction	-5.7^o	12.7^o	0.19
Velocity vector magnitude	0.16 m/s	0.26 m/s	0.39
Turbulent Kinetic Energy	0.09 m^2/s^2	0.13 m^2/s^2	0.98

Table 4: Global comparison of simulation and measurement at the 16 points of interest through statistical performances scores

It can be highlighted that, for almost all of the considered points, the predicted flow direction obtained from CFD turbulent simulation is in good agreement with the measured flow direction. Indeed, RMSE score on the horizontal flow direction is about 12^o and the associated NRMSE score is less than 0.2. The limited exceptions appear when the flow velocity is not significant, *i.e.* less than 0.5 m/s, as for the point P3. However, the CFD simulation rightly predicts that the point P3 corresponds to a dead zone flow. Even though the flow direction is well predicted, we can point out from table 4 that the simulated flow velocity over-estimates the measured flow velocity (BIAS score of 0.16 m/s). In fact, in the Sense-City urban area, the presence of some geometrical details (not considered in the model geometry) like antennas, panels, traffic lights, stairs near the building, air quality sensors, may slow down the airflow when it encounters these obstacles. The error between the simulated and the measured velocities magnitude goes from 0.05 m/s for the point P14 to 0.49 m/s for the point P13 and the RMSE score is of 0.26 m/s. These gaps can be explained by several reasons :

- **geometry simplification** of the multiple holes in the forced-air ducts by rectangular slots;
- **inaccuracy of the inlet/outlet boundary conditions** of the CFD problem due to the measurement errors in the first serie of measurements using the 1D hot wire anemometer;
- **discretization error** as we wanted a good compromise between computational cost and numerical solution accuracy;
- **model error** coming from the URANS model with the $k-$omega SST turbulence model;
- **measurement error** of the 3D ultrasonic anemometer and other sources of errors in the placement and the orientation of the *CSAT-3B* sensor.

But globally, if we are interested to capture the global behavior of the flow velocity, the simulation results are satisfying.

Finally, the comparison between simulated and measured TKE at the points of interest is represented in figure 11. As for the velocity, the simulation overestimates the measured values of k for most of the considered points. Even if important gap between simulation and measured TKE can be observed in figure

11 and in table 4, the order of magnitude and the trends are acceptable. Indeed, high turbulent kinetic energies are observed at points P4, P6, P7 and P10 in both the measurement and the simulation.

6. Conclusions and Perspectives

In this work, we present a CFD analysis of the 3D turbulent airflow of an original urban area consisting on a real-scale urban district under a climate-controlled environment named "Sense-City". A grid convergence study is made to select an appropriate coarse mesh for the URANS simulation, namely a mesh enabling fast computation without a significant loss in the accuracy of the numerical solution. The results of the numerical analysis are compared with experimental measurements collected at a pedestrian level of 1.5 m from the ground using a 3D ultrasonic anemometer. Despite the use of a coarse computational grid and the uncertainties on the boundary conditions, the numerical analysis gives a relevant prediction of the general behaviour of the airflow in the *mini-city 1* within the Sense-City climatic chamber. It provides the main characteristics of the airflow pattern such as the flow direction and dead flow zones. In future works, model reduction combined with data assimilation are to be implemented to improve the accuracy of the simulated airflow without increasing the computational cost. Besides, the simulated flow will be used for air quality purposes at the district scale, *e.g.* validation of a transport-diffusion-reaction model for pollutants cartography using gas sensors, outdoor/indoor pollution transfer and design of depolluting system using virtual testing strategy.

7. Acknowledgments

The authors acknowledge the support from the project Sense-City funded by ANR (France) within the Investment for the Future Program under reference number ANR-10-EQPX-48. They also thank the Sense-City team especially Erick Merliot and Philippe Bruley for their help during the measurement campaign in Sense-City.

References

[1] J. Ahrens, B. Geveci, and C. Law. *ParaView: An End-User Tool for Large Data Visualization.* Vizualisation Handbook, Elsevier, 2005.

[2] A. Alonso-Estebanez, P. Pascual-Munoz, C. Yague, R. Laina, and D. Castro-Fresno. Field experimental study of traffic-induced turbulence on highways. *Atmospheric Environment*, 61:189–196, 2012.

[3] F. Archambeau, N. Méchitoua, and M. Sakiz. Code Saturne: A Finite Volume Code for the computation of turbulent incompressible flows -Industrial Applications. *International Journal on Finite Volumes*, 1, 2004.

[4] M. Balczo, C. Gromke, and B. Ruck. Numerical modeling of flow and pollutant dispersion in street canyons with tree planting. *Meteorologische Zeitschrift*, 18(2, SI):197–206, 2009.

[5] C. Beauchene, N. Laudinet, F. Choukri, J. L. R., S. Benhamadouche, J. Larbre, M. Chaouat, M. Benbunan, M. Mimoun, J. P. Lajonchere, V. Bergeron, and F. Derouin. Accumulation and transport of microbial-size particles in a pressure protected model burn unit: CFD simulations and experimental evidence. *BMC Infectious Diseases*, 11, 2011.

[6] B. Blocken. Computational Fluid Dynamics for urban physics: Importance, scales, possibilities, limitations and ten tips and tricks towards accurate and reliable simulations. *Building and Environment*, 91:219–245, 2015.

[7] B. Blocken and J. Persoon. Pedestrian wind comfort around a large football stadium in an urban environment: CFD simulation, validation and application of the new Dutch wind nuisance standard. *Journal of wind engineering and industrial aerodynamics*, 97(5-6):255–270, 2009.

[8] F. Carbajo Fuertes, G. Valerio Iungo, and F. Porte-Agel. 3d turbulence measurements using three synchronous wind lidars: Validation against sonic anemometry. *Journal of Atmospheric and Oceanic Technology*, 31(7):1549,Äì–1556, 2014.

[9] I. B. Celik, U. Ghia, P. J. Roache, C. J. Freitas, H. Coleman, and P. E. Raad. Procedure for Estimation and Reporting of Uncertainty Due to Discretization in CFD Applications. *J. Fluids Eng.*, 130(7), 2008.

[10] R. Chakir, Y. Maday, and P. Parnaudeau. A non-intrusive reduced basis approach for parametrized heat transfer problems. *Journal of Computational Physics*, 376:617–633, 2019.

[11] Y. Delarablée. *Intégration thermique et mécanique des géostructures énergétiques : de l'échelle du bâtiment à l'échelle de la cité (in French)*. PhD thesis, Université Paris-Est, 2019.

[12] S. Di Sabatino, R. Buccolieri, B. Pulvirenti, and R. E. Britter. Flow and pollutant dispersion in street canyons using FLUENT and ADMS-Urban. *Environmental Modeling & Assessment*, 13(3):369–381, 2008.

[13] Z. Djatouti, J. Waeytens, P. Chatellier, and L. Chamoin. Goal-oriented sensor placement and model updating strategies applied to a real building in the Sense-City equipment under controlled winter and heat wave scenarios. *Energy and Buildings*, 231:110486, 2021.

[14] L. Dong, H. Zuo, L. Hu, B. Yang, L. Li, and L. Wu. Simulation of heavy gas dispersion in a large indoor space using CFD model. *Journal of Loss Prevention in the Process Industries*, 46:1–12, 2017.

[15] A. Fathy, M. Le Pivert, Y. J. Kim, M. O. Ba, M. Erfan, Y. M. Sabry, D. Khalil, Y. Leprince-Wang, T. Bourouina, and M. Gnambodoe-Capochichi. Continuous Monitoring of Air Purification: A Study on Volatile Organic Compounds in a Gas Cell. *Sensors*, 20(3), 2020.

[16] J. Franke, A. Hellsten, H. Schlunzen, and B. Carissimo. Best Practice Guideline for the CFD Simulation of Flows in a Urban Environment : COST Action 732 Quality Assurance and Improvement of Microscale Meteorological Models. *Meteorological Inst.*, 2007.

[17] P. Gousseau, B. Blocken, T. Stathopoulos, and G. J. F. van Heijst. CFD simulation of near-field pollutant dispersion on a high-resolution grid: A case study by LES and RANS for a building group in downtown Montreal. *Atmospheric Environment*, 45(2):428–438, 2011.

[18] C. Gromke, B. Blocken, W. Janssen, B. Merema, T. van Hooff, and H. Timmermans. CFD analysis of transpirational cooling by vegetation: Case study for specific meteorological conditions during a heat wave in Arnhem, Netherlands. *Building and Environment*, 83(SI):11–26, 2015.

[19] C. Gromke, R. Buccolieri, S. Di Sabatino, and B. Ruck. Dispersion study in a street canyon with tree planting by means of wind tunnel and numerical investigations - Evaluation of CFD data with experimental data. *Atmopheric Environment*, 42(37):8640–8650, 2008.

[20] J. K. Hammond and R. Chakir. A non-intrusive reduced order data assimilation method applied to the monitoring of urban flows. In *CSMA2019 - 14ème Colloque National en Calcul des Structures, Presqu'île de Giens, France*, 2019.

[21] J. K. Hammond Hammond, R. Chakir, F. Bourquin, and Y. Maday. Pbdw: A non-intrusive reduced basis data assimilation method and its application to an urban dispersion modeling framework. *Applied Mathematical Modelling*, 76:1–25, 2019.

[22] J. Hang, Y. Li, and M. Sandberg. Experimental and numerical studies of flows through and within high-rise building arrays and their link to ventilation strategy. *Journal of wind engineering and industrial aerodynamics*, 99(10):1036–1055, 2011.

[23] F. Hecht. New development in freefem++. *J. Numer. Math.*, 20(3-4):251–265, 2012.

[24] S. Hussain, P. H. Oosthuizen, and A. Kalendar. Evaluation of various turbulence models for the prediction of the airflow and temperature distributions in atria. *Energy and Buildings*, 48:18–28, 2012.

[25] Sousa J., C. Garcia-Sanchez, and C. Gorle. Improving urban flow predictions through data assimilation. *Building and Environment*, 132:282–290, 2018.

[26] W. P. Jones and B. E. Launder. The prediction of laminarization with a two-equation model of turbulence. *Int. J. of Heat and Mass Transfer*, 15(2):301–314, 1972.

[27] K. Kosutova, T. van Hooff, C. Vanderwel, B. Blocken, and J. Hensen. Cross-ventilation in a generic isolated building equipped with louvers: Wind-tunnel experiments and cfd simulations. *Building and Environment*, 154:263 – 280, 2019.

[28] N. Koutsourakis, J. G. Bartzis, and N. C. Markatos. Evaluation of Reynolds stress, k-epsilon and RNG k-epsilon turbulence models in street canyon flows using various experimental datasets. *Environmental Fluid Mechanics*, 12(4):379–403, 2012.

[29] M. Le Pivert, R. Poupart, M. Capochichi-Gnambodoe, N. Martin, and Y. Leprince-Wang. Direct growth of ZnO nanowires on civil engineering materials: smart materials for supported photodegradation. *Microsystems & Nanoengineering*, 5, 2019.

[30] X. X. Li, C. H. Liu, D. Y. C. Leung, and K. M. Lam. Recent progress in CFD modelling of wind field and pollutant transport in street canyons. *Atmospheric Environment*, 40(29):5640–5658, 2006.

[31] A. Limane, H. Fellouah, and N. Galanis. Simulation of airflow with heat and mass transfer in an indoor swimming pool by OpenFOAM. *International Journal of Heat and Mass Transfer*, 109:862–878, 2017.

[32] L. Liptak, E. Fojcikova, and P. Carny. Comparison of the este cbrn model with the joint urban 2003 experiment. *Boundary-Layer Meteorol*, 171:439–464, 2019.

[33] F. R. Menter. Zonal Two Equation $k-\omega$ Turbulence Models for Aerodynamic Flows. *AIAA Journal*, 1993.

[34] B. Mohammadi and O. Pironneau. *Analysis of the k-epsilon turbulence model*. Wiley, 1994.

[35] H. Montazeri and B. Blocken. CFD simulation of wind-induced pressure coefficients on buildings with and without balconies: Validation and sensitivity analysis. *Building and Environment*, 60:137–149, 2013.

[36] J. I. Peren, T. van Hooff, B. C. C. Leite, and B. Blocken. CFD analysis of cross-ventilation of a generic isolated building with asymmetric opening positions: Impact of roof angle and opening location. *Building and Environment*, 85:263–276, 2015.

[37] R. Ramponi, B. Blocken, L. B. De Coo, and W. D. Janssen. CFD simulation of outdoor ventilation of generic urban configurations with different urban densities and equal and unequal street widths. *Building and Environment*, 92:152–166, 2015.

[38] A. Ribes and C. Caremoli. Salome platform component model for numerical simulation. In *COMPSAC 07: Proceeding of the 31st Annual International Computer Software and Applications Conference*, pages 553–564, Washington, DC, USA, 2007. IEEE Computer Society.

[39] T. Rigaut. *Time decomposition methods for optimal management of energy storage under stochasticity*. PhD thesis, Université Paris-Est, 2019.

[40] S. Rodriguez. *Applied Computational Fluid Dynamics and Turbulence Modeling*. Springer Nature Switzerland, 2019.

[41] P. Sagaut. *Large Eddy Simulation for Incompressible Flows*. Springer-Verlag Berlin Heidelberg, 2006.

[42] S. M. Salim, S. C. Cheah, and A. Chan. Numerical simulation of dispersion in urban street canyons with avenue-like tree plantings: Comparison between RANS and LES. *Building and Environment*, 46(9):1735–1746, 2011.

[43] Y. Shi, F. Hu, G. Fan, and Z. Zhang. Multiple technical observations of the atmospheric boundary layer structure of a red-alert haze episode in beijing. *Atmospheric Measurement Techniques*, 12(9):4887–4901, 2019.

[44] E. Solazzo, X. Cai, and S. Vardoulakis. Modelling wind flow and vehicle-induced turbulence in urban streets. *Atmospheric Environment*, 42(20):4918–4931, 2008.

[45] J. Waeytens, S. Durand, and S. Sadr. Experimental validation of a CFD-based air quality sensor placement strategy to localize indoor source emissions. In *Proceedings of Building Simulation 2019: 16th Conference of IBPSA, Rome, Italy*. International Building Performance Simulation Association, 2019.

[46] J. Waeytens and S. Sadr. Computer-aided placement of air quality sensors using adjoint framework and sensor features to localize indoor source emission. *Building and Environment*, 144:184–193, 2018.

[47] X. Wei, E. Dupont, E. Gilbert, L. Musson-Genon, and B. Carissimo. Experimental and numerical study of wind and turbulence in a near-field dispersion campaign at an inhomogeneous site. *Boundary-Layer Meteorol*, 160:475–499, 2016.

[48] D. C. Wilcox. *Turbulence Modeling for CFD*. DCW Industries, Inc., 1994.

[49] D. C. Wilcox. Formulation of the $k-\omega$ Turbulence Model Revisited. *AIAA Journal*, 46(11), 2008.

[50] M. F. Yassin. Impact of height and shape of building roof on air quality in urban street canyons. *Atmospheric Environment*, 45(29):5220–5229, 2011.

Appendix

In the appendix, we give the definition of the statistical performances scores used in section 5 for the comparison of the numerical simulation with the experimental data.

- BIAS = $\overline{s-o}$
- RMSE (Root Mean Square Error)= $\sqrt{\overline{(s-o)^2}}$
- NRMSE = $\dfrac{RMSE}{\overline{o}}$

where s stands for *simulated* values and o for *observed* values with $\overline{\mathrm{x}} = \dfrac{1}{n}\sum_{i=1}^{n} \mathrm{x}(p_i)$ for the average over the dataset.